

Impacts of Topographic Complexity on Modeling Moisture Transport and Precipitation over the Tibetan Plateau in Summer[※]

Gudongze LI¹, Haoming CHEN¹, Mingyue XU¹, Chun ZHAO^{*1,2,3},
Lei ZHONG¹, Rui LI¹, Yunfei FU¹, and Yanhong GAO⁴

¹School of Earth and Space Sciences, University of Science and Technology of China, Hefei 230026, China

²CAS Center for Excellence in Comparative Planetology, University of Science and Technology of China, Hefei 230026, China

³Frontiers Science Center for Planetary Exploration and Emerging Technologies, University of Science and Technology of China, Hefei 230026, China

⁴Department of Atmospheric and Oceanic Sciences & Institute of Atmospheric Sciences, Fudan University, Shanghai 200433, China

(Received 4 November 2021; revised 11 January 2022; accepted 28 January 2022)

ABSTRACT

The non-hydrostatic global variable resolution model (MPAS-atmosphere) is used to conduct the simulations for the South Asian Summer monsoon season (June, July, and August) in 2015 with a refinement over the Tibetan Plateau (TP) at the convection-permitting scale (4 km). Two experiments with different topographical datasets, complex (4-km) and smooth (60-km) topography, are designed to investigate the impacts of topographical complexity on moisture transport and precipitation. Compared with the observations and reanalysis data, the simulation can successfully capture the general features of key meteorological fields over the TP despite slightly underestimating the inflow through the southern TP. The results indicate that the complex topography can decrease the inward and outward moisture transport, ultimately increasing the total net moisture transport into the TP by ~11%. The impacts of complex topography on precipitation are negligible over the TP, but the spatial distributions of precipitation over the Himalayas are significantly modulated. With the inclusion of complex topography, the sharper southern slopes of the Himalayas shift the lifted airflow and hence precipitation northward compared to the smooth topography. In addition, more small-scale valleys are resolved by the inclusion of complex topography, which serve as channels for moisture transport across the Himalayas, further favoring a northward shift of precipitation. Overall, the difference between the two experiments with different topography datasets is mainly attributed to their differing representation of the degree of the southern slopes of the Himalayas and the extent to which the valleys are resolved.

Key words: convection-permitting simulation, Tibetan Plateau, complex topography, moisture transport, precipitation

Citation: Li, G. D. Z., H. M. Chen, M. Y. Xu, C. Zhao, L. Zhong, R. Li, Y. F. Fu, and Y. H. Gao, 2022: Impacts of topographical complexity on modeling moisture transport and precipitation over the Tibetan Plateau in summer. *Adv. Atmos. Sci.*, **39**(7), 1151–1166, <https://doi.org/10.1007/s00376-022-1409-7>.

Article Highlights:

- Global variable-resolution simulation at convection-permitting scale can reproduce key meteorological fields over the TP in summer.
- Topographical complexity reduces the inward/outward wind flow of the TP thereby increasing the net moisture transport into the TP by ~11%.
- Differences in precipitation due to topography result from the different extents of the resolved southern slopes and valleys of the Himalayas.

1. Introduction

The Tibetan Plateau (TP), known as the world's third pole (Qiu, 2008), is a large land feature with an average elevation of over 4 km and an area of 2.5×10^6 km². The uplif-

※ This paper is a contribution to the special issue on Third Pole Atmospheric Physics, Chemistry, and Hydrology.

* Corresponding author: Chun ZHAO
Email: chunzhao@ustc.edu.cn

ted area exerts significant dynamic and thermal effects on the large-scale atmospheric circulation through its momentum and energy exchange with the atmosphere (e.g., Ye and Wu, 1998; Duan and Wu, 2005; Wu et al., 2007, 2012, 2015; Boos and Kuang, 2010, 2013; Zhao et al., 2019c). The TP is also the headwater area for many large Asian rivers (e.g., Singh and Bengtsson, 2004; Barnett et al., 2005; Immerzeel et al., 2010; Lutz et al., 2014) and hence plays an important role in the water cycle. Precipitation changes over the TP are critical to glacier mass balance, runoff of rivers, and ecology (e.g., Yang et al., 2011; Yao et al., 2012; Gao et al., 2014, 2015; Shen et al., 2015). Over the TP, the precipitation reaches its annual maximum in summer mainly due to the water vapor transport (WVT) driven by the South Asian summer monsoon (SASM), which can significantly affect the precipitation distribution over the TP (e.g., Yanai and Wu 2006; Xu et al., 2008; Feng and Zhou 2012; Zhang et al., 2012). Therefore, to prevent drought and flood episodes in downstream regions, it is important to understand the mechanisms that drive moisture transport and precipitation processes over the TP in summer.

Numerical models have been widely used to investigate the moisture budget and precipitation variations over the TP. However, it remains a challenge for current atmospheric models to simulate the precipitation and circulation over the TP accurately. Analysis of modeling results from the Coupled Model Intercomparison Project (CMIP3, CMIP5, and CMIP6) showed that precipitation amounts over the TP tended to be significantly overestimated (Xu et al., 2010; Zhu and Yang, 2020; Li et al., 2021). Only half of the 24 models available in CMIP5 could reproduce the observed seasonal variations for precipitation (Su et al., 2013). Gu et al. (2020) assessed the performance of the Regional Climate Model (RegCM4) over the TP and concluded that most model configurations could not well depict the seasonal and interannual variations of precipitation. One factor contributing to these biases/uncertainties may be associated with the complex topography around the TP.

The Himalayan region is well known as the main WVT passageway from the Indian Ocean to the TP (e.g., Tian et al., 2007; Feng and Zhou, 2012; Zhang et al., 2017). However, the Himalayan region, on the edge of TP with steep slopes, is often regarded as an obstacle to the WVT. At the same time, many meridional valleys along the Himalayas may act as water vapor passageways in this region (e.g., Burbank et al., 2012). Due to the complex topography of the Himalayas, previous studies have found that model resolution was a key factor that can significantly affect the simulation results of moisture and tracer transport and precipitation over the TP (e.g., Karki et al., 2017; Lin et al., 2018; Xu et al., 2018; Rahimi et al., 2019; Wang et al., 2020; Zhang et al., 2020). Xu et al. (2018) used a regional climate model to investigate the role of horizontal resolution on moisture transport and precipitation over the TP. They found that in a simulation with a relatively coarser resolution of 50 km, the smoothed mountain slope could lift the water vapor to

the TP easier than the one with 25 km resolution, which had the net effect of increasing the precipitation in the southern TP. Rahimi et al. (2019) conducted numerical experiments at multiple resolutions [(1/8° to 1°] with the global variable-resolution model (VR-CESM). They investigated the relationship between the location of the precipitation peak along the slope and the horizontal resolution and found that finer resolution could shift the peak location northward. Overall, the complex terrain of TP cannot be resolved well in coarse-resolution simulations, which could result in modeling biases of the moisture and tracer transport over the TP and its surrounding areas (e.g., Ma et al., 2015; Zhou et al., 2017; Lin et al., 2018; Zhang et al., 2020).

Although increasing the horizontal resolution to 10–20 km can improve the modeling results of WVT and precipitation, previous studies found that the orographic drag of complex topography may only be resolved at horizontal resolutions of a few kilometers or even finer (e.g., Xue et al., 2011; Sandu et al., 2016; Wang et al., 2020). In addition, simulations at resolutions of tens of kilometers need convective parameterizations that may also introduce large uncertainties in simulating convective systems and thus large-scale circulation during the summer monsoon season (e.g., Zhao et al., 2019b; Xu et al., 2021). Therefore, some studies conducted numerical experiments using regional models at convection-permitting scales (a few kilometers or finer) over the TP and its surrounding areas to better capture the effect of complex topography and its associated moisture transport and precipitation processes (e.g., Karki et al., 2017; Lin et al., 2018; Wang et al., 2020). Karki et al. (2017) investigated the skill of convection-permitting simulations over the central Himalayas and suggested that high-resolution (5 km and 1 km) simulations can produce more realistic monsoonal precipitation to include its nocturnal peak. Lin et al. (2018) conducted multiple regional modeling experiments over the central Himalayas with different resolutions (from 30 km to 2 km) and found that finer terrain could decrease the wind speed and WVT through the Himalayas in summer. Additionally, the impacts of topographic complexity on transport were also investigated by applying a sub-grid topography parameterization scheme in the simulations (e.g., Xue et al., 2011; Sandu et al., 2016; Wang et al., 2020). For example, Wang et al. (2020) found a reduction in precipitation at higher elevations along the southern slopes of the TP but an increase at lower elevations as a result of using either finer horizontal resolution or coarser horizontal resolution with the parameterization of turbulent orographic form drag (TOFD) in the Central Himalaya Mountains (CHM). They concluded that TOFD helps to reduce the wet bias of simulated precipitation over the CHM. These studies found that TOFD is an important factor affecting the WVT and precipitation over the Himalayan region and the TP. However, simulations with resolutions of only a few kilometers may better resolve the TOFD and thus reduce the WVT from the Indian Ocean to the TP and the subsequent precipitation over the central Himalayas.

Although a regional model can investigate WVT and precipitation over the Himalayas and the TP at convection-permitting scales, previous studies mainly conducted simulations over relatively small regions. With limited-area simulations, the impacts of the complex topography of the Himalayas on WVT and precipitation over the entire TP cannot be fully assessed. In addition, the limited-area simulation may also not be adequate to fully simulate the impacts of complex topography on the large-scale circulation and thus the WVT to the TP due to the constraint of lateral boundaries. Therefore, in this study, a non-hydrostatic global variable-resolution atmospheric model, the Model for Prediction Across Scales (MPAS-Atmosphere) (Ringler et al., 2008; Skamarock et al., 2012), is used to simulate moisture transport and precipitation over the TP at convection-permitting scales during the SASM. The MPAS-Atmosphere simulations open opportunities for convection-permitting simulations with regional refinement. Compared to global convection-permitting modeling, the computational cost is significantly reduced, and the lateral boundary constraint is avoided. Fine-scale features can be better resolved in the regions of interest, and uncertainties within convective parameterizations can be reduced over the refined regions (e.g., Zhao et al., 2019b; Xu et al., 2021).

To date, few studies have used non-hydrostatic global variable-resolution models, with refinement at convection-permitting scales, to investigate the impacts of topographical complexity on moisture transport and precipitation over the TP. This study aims to (1) generally evaluate the global simulations of related meteorological fields around TP with refinement at the convection-permitting scale and (2) investigate the impacts of topographic complexity on the moisture transport and precipitation over the TP. The remainder of this paper is as follows. Section 2 will concentrate on the model description and numerical experimental design, followed by the evaluation of key meteorological fields around the TP in section 3. In section 4, the impacts of topographic complexity on moisture transport and precipitation over the TP are investigated. A conclusion and discussion will be given in section 5.

2. Methodology

2.1. Model description

2.1.1. MPAS-Atmosphere (MPAS-A) model

The MPAS model (v7.0), characterized by a non-hydrostatic dynamical core and a C-grid horizontally discretized scheme, was used in this study (Skamarock et al., 2012). The global variable-resolution meshes were generated by unstructured spherical centroidal Voronoi tessellation (SCVT) generation algorithms (Ringler et al., 2011). The vertical coordinate and temporal discretization were similar to the Weather Research and Forecasting (WRF) model (Skamarock and Klemp, 2008). Additional details can be found in Klemp (Klemp et al., 2007; Klemp, 2011). The list

of physics schemes available in this version of MPAS was generally introduced in Zhao et al. (2019b) and Xu et al. (2021). In the past few years, the MPAS model has been widely applied to study many important scientific questions related to the resolution dependency of clouds and precipitation, precipitation extremes, atmospheric rivers, etc. (e.g., O'Brien et al., 2013, 2016; Landu et al., 2014; Yang et al., 2014; Hagos et al., 2015; Sakaguchi et al., 2015, 2016; Zhao et al., 2016, 2019b; Judt, 2018; Xu et al., 2021).

2.1.2. Numerical experiments

This study focuses on the SASM season from 1 June to 31 August (JJA) in 2015. Two numerical experiments are conducted, configured at a 4–60 km global variable resolution. Figure 1 shows the mesh configuration of the simulations. The refined region with a cell size of 4 km is centered over the TP and its surrounding area and is encircled by the solid line. The cell size gradually increases to approximately 60 km outside the dotted circular line. One experiment utilizes the original terrain dataset at 4–60 km resolution, while the other uses the terrain dataset at 60 km uniform resolution. The two experiments are referenced by the simulations with complex and smooth topography over the TP, respectively, hereafter V4km and V4km.smooth. More specifically, the V4km.smooth is conducted with the same configuration as V4km except that the terrain heights of the refined and transition regions are bilinearly interpolated from the terrain heights at 60 km resolution (e.g., Lin et al., 2018; Zhang et al., 2020). In this way, the impacts of terrain complexity over the refined region can be examined by subtracting the

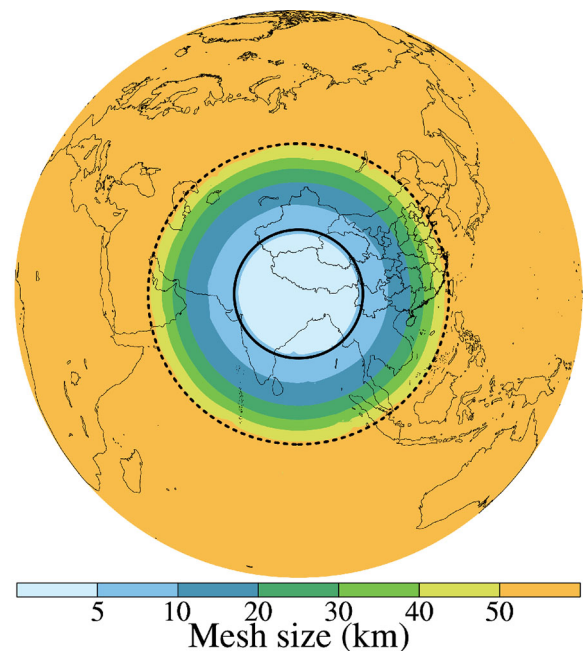


Fig. 1. Global variable-resolution mesh size distribution in the variable-resolution 4–60 km experiment. The area encircled by the solid line is consistent with a roughly 4 km mesh size, the area outside the dotted line is consistent with a roughly 60 km mesh size, and the area in between is the transition zone.

result from using V4km.smooth from that of V4km. Figure 2 shows the spatial distributions of terrain height surrounding the TP from the V4km and V4km.smooth experiments. Obviously, the terrain is much smoother in V4km than in V4km.smooth. The mountain ridges and valleys of the Himalayas are better resolved in V4km but are mostly missed or underestimated in V4km.smooth. The difference in terrain height between the two experiments is significant along the Himalayas [Fig. S1 in the electronic supplementary material (ESM)]. The area surrounded by five dashed lines is defined as the TP region, the focus of further analysis in this study. The five dashed lines (B1–B5) denote the five lateral boundaries used for moisture transport estimation in section 4.

The model is configured to have 55 vertical layers with the top of the model at 30 km above the surface. Both experiments use the scale-aware convective parameterization GF, the Thompson cloud microphysics scheme (Thompson et al., 2008), the YSU planetary boundary layer scheme (Hong and Lim, 2006; Hong, 2010), the Noah land surface scheme (Chen and Dudhia, 2001), and the RRTMG short and long-wave radiation schemes (Mlawer et al., 1997; Iacono et al., 2000). The initial condition is derived from the European Centre for Medium-Range Weather Forecasts (ECMWF) Reanalysis (ERA-Interim) at a 0.25° horizontal grid spacing and 37 vertical levels. The simulations are conducted continuously for every five days and initialized at 00 UTC for 120 hours to produce reasonable meteorological fields. To avoid the impact of the initial spin-up period, the results of the first 24 hours are excluded. The simulation results for 24 to 120 hours are analyzed.

2.2. Observation and Reanalysis

Observation and reanalysis datasets are used to evaluate the simulations in this study. The precipitation datasets are obtained from the ERA5 reanalysis and the APHRODITE (Asia Precipitation Highly Resolved Observational

Data Integration Towards Evaluation of water resources) dataset. The APHRODITE dataset obtains long-term daily gridded precipitation and temperature data from rain-gauge observation records over Asia through international collaborations with local meteorological/hydrological agencies and researchers (Yatagai et al., 2008, 2012). The precipitation data provided by APHRODITE is at a 0.25° horizontal resolution and 1-day temporal intervals. The ERA5 reanalysis has atmospheric quantities at a 0.25° horizontal resolution, 37 vertical levels, and 1-hour temporal resolution (Hersbach et al., 2020). The JRA55 (Japanese 55-year Reanalysis) dataset (Kobayashi et al., 2015) is also used as a reference that is reliable over the TP area (Zhao and Zhou, 2020). The JRA55 dataset is produced by the Japan Meteorological Agency (JMA) using a sophisticated data assimilation (DA) system and a newly prepared dataset of past observations, covering the 55 years from 1958 to the present. The JRA55 provides atmospheric fields at a 1.25° horizontal resolution, 37 vertical levels, and 1-hour temporal resolution. In addition, the CRA-40 is the first generation global atmosphere and land reanalysis data released by the China Meteorological Administration with a horizontal resolution of 0.312° and 64 vertical levels, covering the period from 1979 to the present (Zhao et al., 2019a). The assimilation of various conventional and satellite observations, especially over East Asia, into CRA-40 enables the observed good agreement with the ERA5 reanalysis (Yu et al., 2021). It even outperforms other reanalysis datasets in evaluating near-surface wind speed changes over China (Shen et al., 2022).

3. Evaluation of key meteorological fields

Model results are compared to the observations and reanalysis data in this section. Geopotential height and wind fields, near-surface temperature, precipitable water, cloud water path, and precipitation are evaluated in sections 3.1–3.5, respectively.

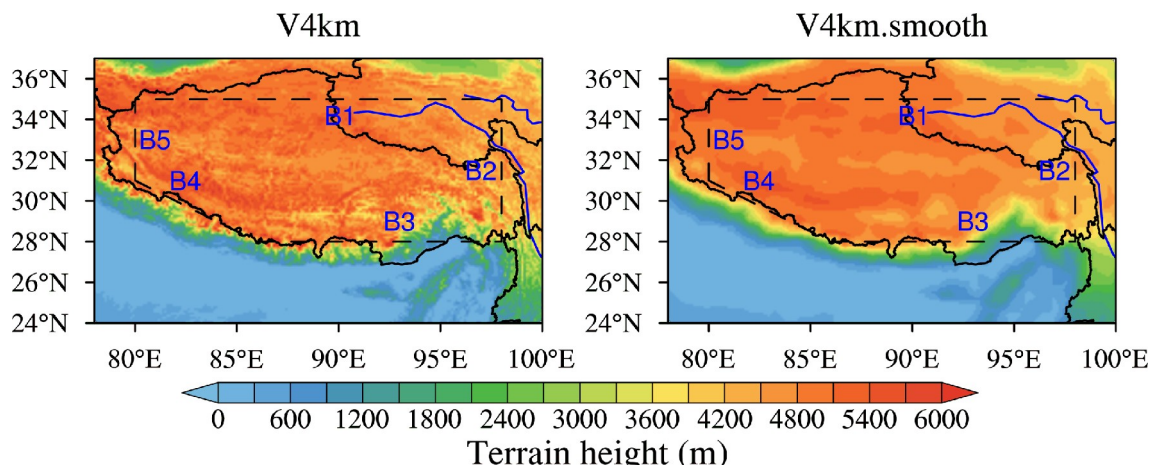


Fig. 2. The spatial distributions of terrain height from the dataset at 4 km resolution with complex topography and smooth topography, which was bilinearly interpolated from the 60 km resolution dataset. Water vapor transport estimation will be calculated on the pentagon enclosed with the dotted lines. The boundaries are named B1–B5, from the north boundary, in clockwise order.

3.1. Geopotential Height and Wind Fields

Figures 3 and 4 show the spatial distributions of the geopotential height and horizontal wind fields at 850 hPa and 500 hPa, respectively, from the ERA5, JRA55, and CRA-40 reanalysis and the V4km simulation averaged for June to August (JJA) of 2015. Both reanalysis datasets show that the geopotential heights at 850 hPa and 500 hPa decrease from the south to the north. At 850 hPa, the V4km simulation reproduces the spatial pattern of geopotential height very well, featuring a flow field dominated by a thermal low in the lower troposphere over the Asian-African continent, which causes westerlies to prevail over India. The TP divides the westerly wind into two branches, one to the south and another to the north, which flows around the TP. The northward wind generates a high-pressure ridge, while the southward wind promotes the generation of the cyclone. During the SASM, there is a cyclonic shear of the prevailing westerlies at $\sim 85^{\circ}\text{E}$, and the closer its location is to the

TP, the sharper the wind direction shift. The flow even turns southeasterly over Northeast India. The Himalayas physically block the winds directed towards the TP. The V4km simulation reproduces this circulation well.

At 500 hPa, the V4km simulation generally produces a similar spatial pattern of the geopotential height but overestimates the magnitudes throughout the region, which is due to the simulated higher temperature from the lower to middle troposphere over the region. Figure 5 shows the spatial distributions of temperature averaged for the atmosphere between 850 hPa and 500 hPa from the ERA5, JRA55, and CRA-40 reanalysis and the V4km simulation averaged for JJA of 2015. The higher temperature in the V4km model run leads to a thicker atmosphere between 850 hPa and 500 hPa and thus a higher geopotential height at 500 hPa than the reanalysis. At 500 hPa, the wind flow from the mid-latitude westerlies at $\sim 42^{\circ}\text{N}$ is broken into the two branches at $\sim 75^{\circ}\text{E}$ by the TP. One branch keeps eastward flow entering through the western boundary of TP, and the other branch turns south-

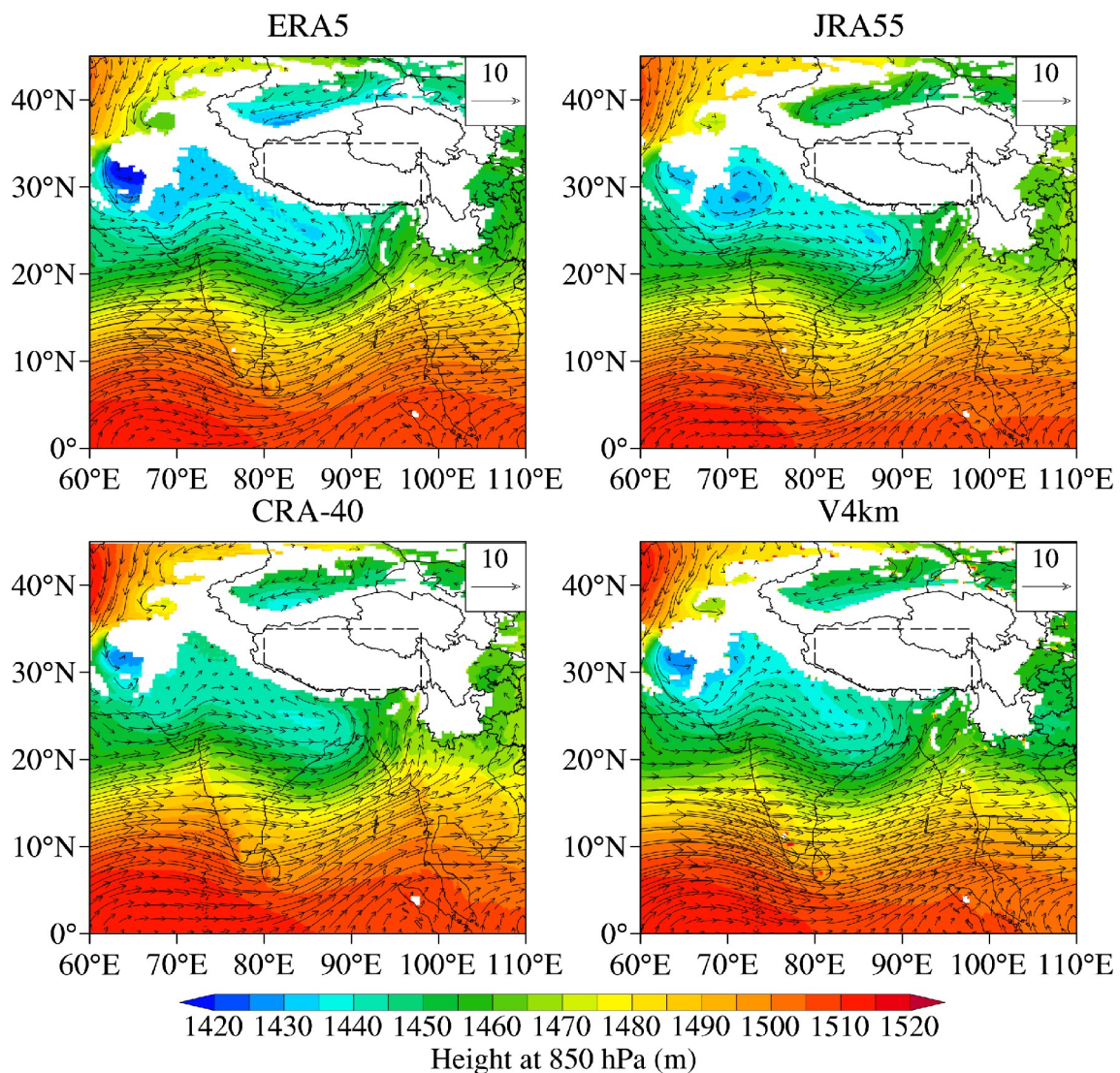


Fig. 3. Spatial distributions of geopotential height and horizontal wind field at 850 hPa from the ERA5, JRA55, and CRA-40 reanalysis and the simulation with the complex topography, averaged from 1 June to 31 August 2015.

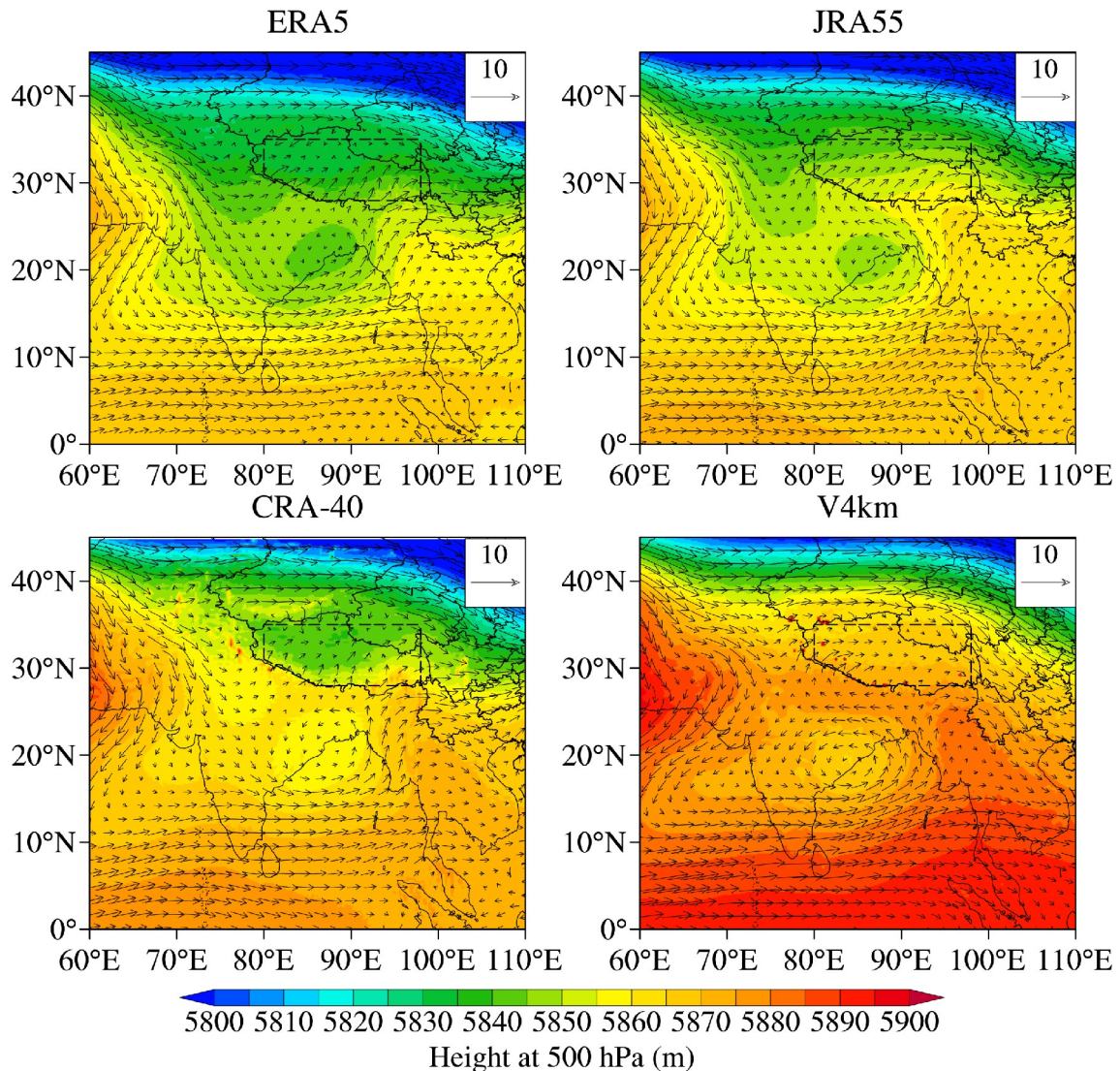


Fig. 4. The spatial distributions of geopotential height and horizontal wind field at 500 hPa from the ERA5, JRA55, and CRA-40 reanalysis and the simulation with the complex topography, averaged for 1 June to 31 August 2015.

eastward. The southeastward branch encounters a low-pressure cyclonic system centered over the Bay of Bengal ($\sim 18^\circ\text{N}$). As a result, the combined flow brings moisture through the southern boundary of TP. In general, the V4km simulation produces a similar spatial pattern of wind fields at 500 hPa, except that the simulated cyclone near the Bay of Bengal is shifted further south compared to the reanalysis, which leads to an underestimated wind flow into the southern TP in the V4km simulation, which may result in less moisture transported across the Himalayas into the TP.

3.2. Two-meter temperature

Figure 6 shows the spatial distributions of the 2-meter temperature from the ERA5 and CRA-40 reanalysis and the V4km simulation averaged for JJA of 2015. The near-surface temperature decreases sharply from North India (above $\sim 30^\circ\text{C}$) to the TP (below 10°C) with a clear “barrier” along the Himalayas. The V4km simulation was generally successful in reproducing the spatial distribution and magnitude of

near-surface temperature, as shown in the reanalyses products. More specifically, the simulation shows better agreement with CRA-40 (ERA5) over North India (over the TP).

3.3. Precipitable Water

Figure 7 shows the spatial distributions of precipitable water from the ERA5, JRA55, and CRA-40 reanalysis and the V4km simulation averaged for JJA of 2015. Both reanalysis datasets consistently show that the largest precipitable water extends from the Bay of Bengal to the foothills of the Himalayas. The values from ERA5 are a little higher than from JRA55 over the region. The precipitable water decreases sharply from North India (above $\sim 40 \text{ kg m}^{-2}$) to the TP (below 10 kg m^{-2}) with a clear “barrier” along the Himalayas. The precipitable water over the TP is much lower than to the south. Over the TP, precipitable water is much lower in the western part than in the eastern part. The V4km simulation reproduces the spatial distributions and magnitudes of precipitable water over the region very well. The

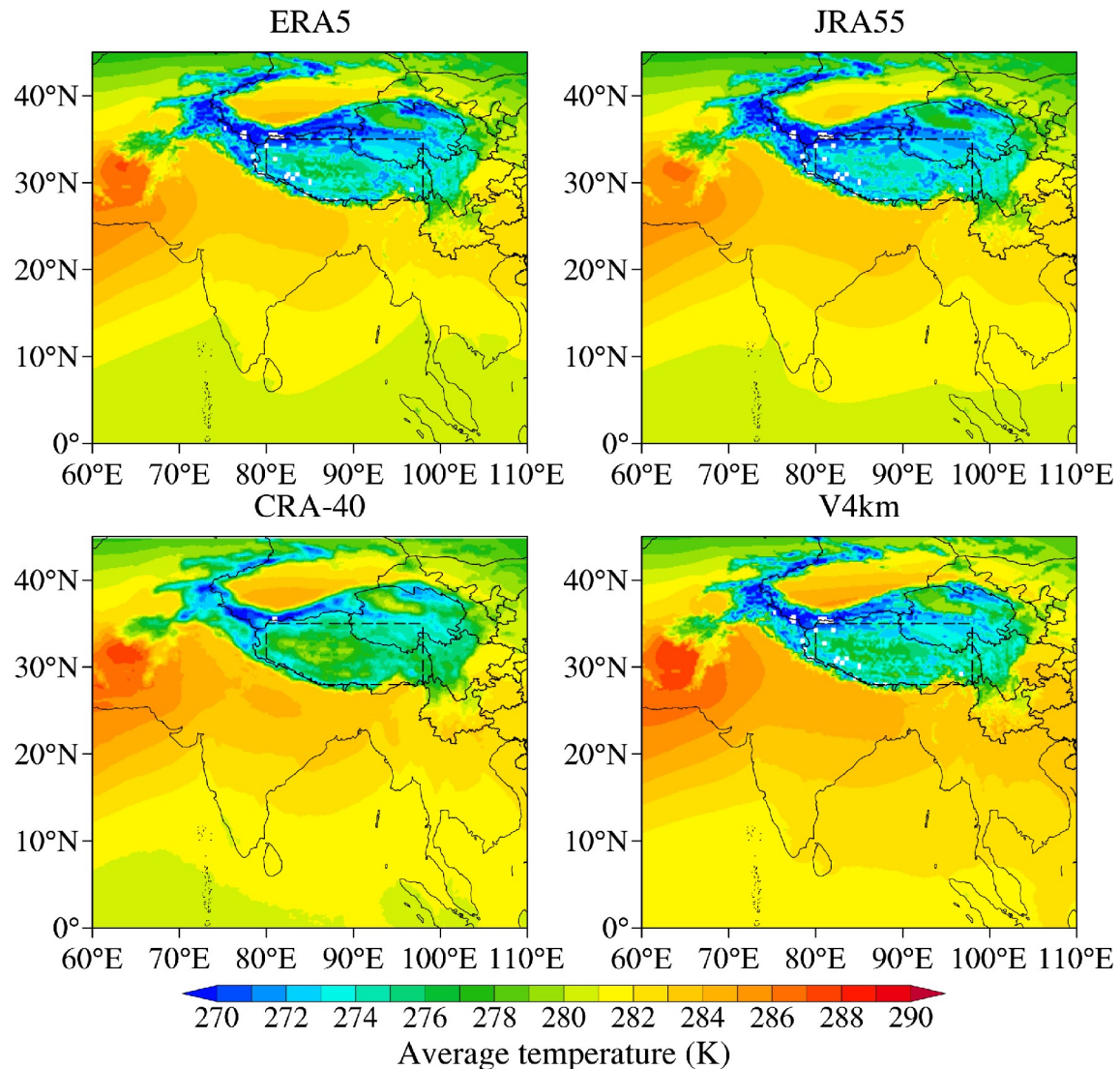


Fig. 5. Spatial distributions of temperature averaged from 500 hPa to 850 hPa from the ERA5, JRA55, and CRA-40 reanalysis, and the simulation with the complex topography averaged from 1 June to 31 August 2015.

simulated results are closest to ERA5 compared to JRA55 and CRA-40, partly because the initial condition of each 5-day forecast is derived from the ERA-Interim reanalysis that may be more consistent with ERA5.

3.4. Cloud Water Path

Figure 8 shows the spatial distributions of cloud water path (including cloud liquid water, ice, and snow) from the ERA5 reanalysis and the V4km simulation, averaged for JJA of 2015. The ERA5 reanalysis shows that clouds concentrate over central India, the northern Bay of Bengal, and the southern slope of the Himalayas. There are also a large amount of clouds over the southeastern TP. The V4km simulation generally captures this spatial distribution of clouds with some deviations. Compared with the reanalysis, the simulation overestimates the cloud amount over the eastern TP while underestimating the cloud amount along the eastern coast of the Bay of Bengal. The simulation produces more clouds over the central Bay of Bengal. Note that clouds

from the reanalysis may also have some uncertainties, especially over areas with complex surface features (e.g., Yao et al., 2020).

3.5. Precipitation

Due to the sparse meteorological stations available over the TP, the overall model performance of simulating precipitation over the TP cannot be fully assessed with station observations. Satellite retrievals of precipitation often have large uncertainties without a sufficient merging of rain gauge observations (Sun et al., 2016). Therefore, the ERA5 and APHRODITE datasets are used to evaluate the modeling results. As mentioned above, APHRODITE is a set of gridded precipitation products based on a dense network of Asian rain-gauge data, including the Himalayas region, to serve as a substitute for station observations (Yatagai et al., 2008). Figure 9 shows the spatial distribution of precipitation from the ERA5 reanalysis, APHRODITE observations, and the V4km simulation averaged for JJA of 2015. The ERA5 reana-

lysis and APHRODITE datasets show high precipitation values over central India, the northern Bay of Bengal, and the southern slope of the Himalayas, consistent with the spatial distribution of clouds. The heavy rainfall band along the

slope of the Himalayas reflects the orographic impact of steep terrain. The precipitation over the TP is much less than that over India due to the blocking of the Himalayas, except that there is an evident intrusion of precipitation over the southeastern TP through the Yarlung Tsangpo Grand Canyon in the eastern Himalayas. The V4km simulation generally captures the main characteristics of precipitation over the TP and surrounding regions. One available station observation of precipitation near the Northern Himalayas is compared with the reanalysis and simulations (not shown). The averaged precipitation of ERA5, APHRODITE, and V4km during the simulation period is 2.90, 2.53, and 2.25 mm d⁻¹, respectively, generally consistent with the observation of 2.59 mm d⁻¹. More station observations over the TP are needed to further evaluate and investigate the simulated precipitation characteristics.

4. Impacts of topographical complexity on moisture transport and precipitation

Due to the important “barrier” effect of the Himalayas on moisture transport and precipitation over the TP, previous studies have examined the impacts of topographical complexity of the Himalayas by analyzing the simulation results with different horizontal resolutions. Although different horizontal resolutions can resolve different scales of topographical complexity, they can also introduce differences in physical processes such as convective clouds. Therefore, this study examines the modeling difference between the V4km and V4km-smooth experiments to reflect the impacts of topographical complexity as discussed below. The convection-permitting resolution at the refinement region covering the entire TP can guarantee reasonably simulated meteorological fields during the SASM season as discussed above and resolve the topographical complexity to a large extent.

4.1. Impacts on moisture transport over the TP

Figure 10 shows the spatial distributions of integrated moisture transport of the V4km over the TP region averaged for JJA of 2015 and the difference between V4km and V4km.smooth. The shaded contour represents the magnitude of moisture transport. It is obvious that the Himalayas diverts the WVT to the TP into two branches, one passage through the southwestern TP and the other through the Yarlung Tsangpo Grand Canyon into the southeastern TP. To quantify the moisture transport through the different pathways into the TP, this study defines the TP as the region within the black box in Fig. 2. The five dashed lines denote the TP’s five boundaries (B1–B5). The estimates of column integrated moisture transport through the five boundaries into the TP averaged for June-August of 2015 are listed in Table 1. It is evident that moisture is transported away from the TP (negative values) through B1 and B2, while it is transported into the TP (positive values) through B3, B4, and B5. The net effect is for moisture to be transported into the TP. Moisture is mainly transported into the TP through B3, con-

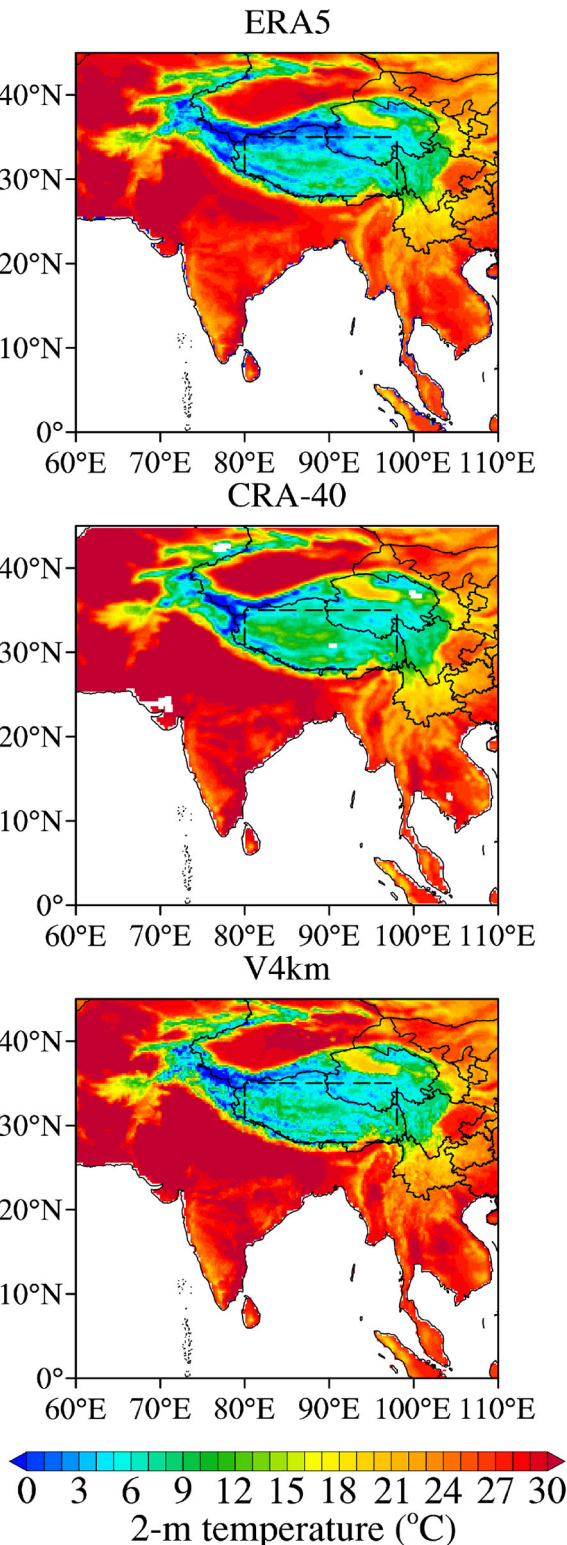


Fig. 6. Spatial distributions of the 2-m temperature from the ERA5, CRA-40 reanalysis, and the simulation with the complex topography averaged from 1 June to 31 August 2015.

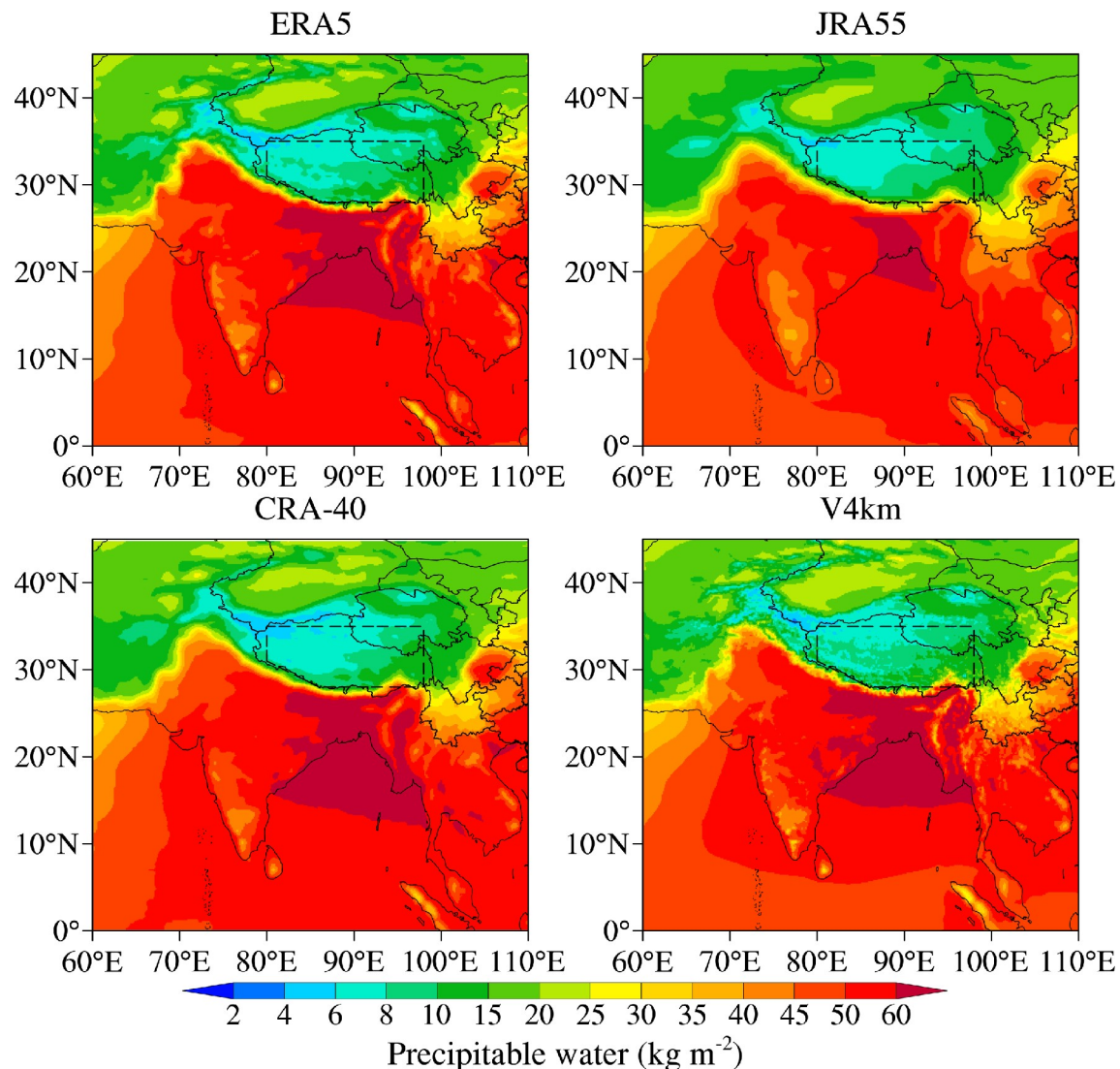


Fig. 7. Spatial distributions of precipitable water from the ERA5, JRA55, and CRA-40 reanalysis and the simulation with the complex topography averaged from 1 June to 31 August 2015.

tributing about ~61% to the total moisture transported into the TP in JJA. The moisture transported from B4 and B5 is comparable, contributing ~23% and ~16%, respectively. The pathway through B2 (~99.8%) dominates the moisture transport away from the TP.

The impact of topographical complexity, i.e., the difference between V4km and V4km.smooth, weakens the moisture transport through the higher mountains and enhances the moisture transport through the deeper valleys such as the Yarlung Tsangpo Grand Canyon (Figs. 10 and S2 in ESM). The overall moisture transport toward the TP through B3, B4, and B5 is weakened by the topographical complexity (Fig. 10), which reduces the moisture transport from 117.9 Tg h^{-1} to 98.9 Tg h^{-1} , from 44.2 Tg h^{-1} to 38.0 Tg h^{-1} , and from 27.4 Tg h^{-1} to 26.1 Tg h^{-1} through B3, B4, and B5, respectively (Table 1). This reduction of moisture transport through the Himalayas is mainly due to the complex topography increasing the surface roughness and weakening the wind fields, consistent with previous studies (e.g.,

Lin et al., 2018; Wang et al., 2020). The analysis shows that the impact of topographical complexity on moisture transport is mainly below 500 hPa (Fig. S2 in ESM). With a global variable-resolution simulation, in addition to the moisture transport across the Himalayas (B3–B5), the transport through other boundaries (B1–B2) can also be examined. Figure 10 shows that the moisture transport away the TP through B1 and B2 is also weakened by the complex topography. The moisture transport away from the TP is reduced from 10.9 Tg h^{-1} to 0.2 Tg h^{-1} and from 124.6 Tg h^{-1} to 103.3 Tg h^{-1} through B1 and B2, respectively. Therefore, the net effect of complex topography on moisture transport into the TP is positive overall, increasing the transport from 54.0 Tg h^{-1} to 59.5 Tg h^{-1} . This result indicates that although the complex topography weakens the moisture transport through the Himalayas, its overall effect increases the net moisture transport into the TP.

Besides the moisture transport, Table 2 shows the moisture budget terms over the TP as denoted in Fig. 2. The

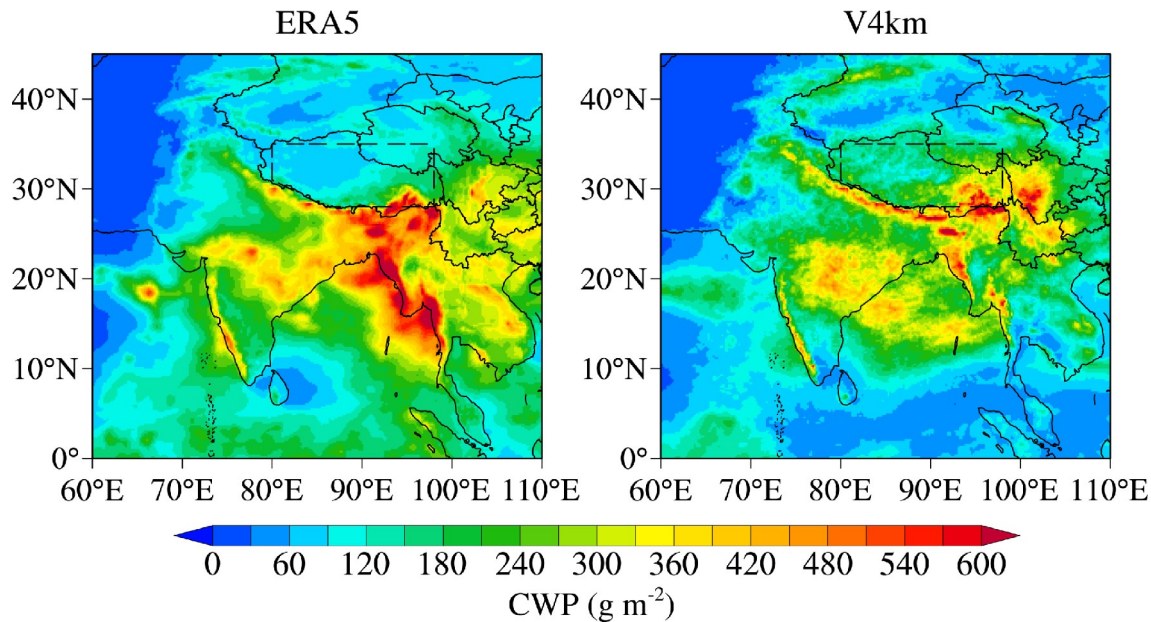


Fig. 8. Spatial distributions of cloud water path (including cloud liquid water, ice, and snow; CWP) from the ERA5 and the simulation with the complex topography averaged from 1 June to 31 August 2015.

impact on the moisture transport term has been discussed above, i.e., the topographical complexity increases the net moisture flow into the TP by $\sim 11\%$ (from 54.0 Tg h^{-1} to 59.5 Tg h^{-1}). The evaporation rate over the TP displays a small increase of $\sim 2\%$ (from 103.6 Tg h^{-1} to 105.8 Tg h^{-1}). The precipitation over the TP is enhanced by $\sim 3\%$ from 186.2 Tg h^{-1} to 192.2 Tg h^{-1} . Therefore, in general, the impacts of topographical complexity on the moisture budget terms over the entire TP are primarily reflected by the moisture transport term, while the impacts on other terms are relatively small. Although the analysis seems to indicate that the impact of topographical complexity on the precipitation of entire TP is small, some previous modeling studies demonstrated that the complex topography might modulate the precipitation around the Himalayas through various other mechanisms, for example, orographic drag (e.g., Karki et al., 2017; Wang et al., 2020). Therefore, the impacts of complex topography on the precipitation are analyzed, focusing on the Himalayas region below.

4.2. Impacts on precipitation over the TP

Figure 11 shows the spatial distributions of difference in precipitation between the V4km and V4km.smooth simulations averaged for JJA of 2015. It shows that the primary impacts of topographical complexity on precipitation concentrate on the Himalayas region, while the precipitation changes within the TP are small. The Himalayan region is further divided into three subregions, western (blue box), central (black box), and eastern (red box) (Fig. 11) for the detailed analysis. The average precipitation over the three subregions is shown in Table 3. Over the western Himalayas, the average precipitation from the V4km simulation is 9.56 mm d^{-1} , slightly less than that from V4km.smooth (9.78 mm d^{-1}). Over the central Himalayas, precipitation is

reduced by about 11% from 11.82 mm d^{-1} (in V4km) to 10.56 mm d^{-1} (in V4km.smooth). Over the eastern Himalayas, the difference between V4km (14.67 mm d^{-1}) and V4km.smooth (14.69 mm d^{-1}) is quite small. Although the difference of average precipitation over the western and eastern Himalayas is relatively small, it is evident that the spatial distributions are significantly modulated by the topographical complexity, which is further investigated below.

Figure 12 shows the precipitation amounts and the terrain heights along the direction perpendicular to the Himalayas for V4km and V4km.smooth averaged over the three subregions. The difference in terrain height between V4km and V4km.smooth is also shown. Over all subregions, precipitation from both simulations mainly concentrates along the slope, with the maxima located at the lower levels of the slope. Precipitation decreases sharply in the upslope direction, consistent with the spatial pattern shown in Fig. 9. Generally, over the western Himalayas, higher terrain leads to higher precipitation in the V4km compared to V4km.smooth. The reduction of precipitation in V4km (e.g., 30.3°N to 30.7°N and 31.2°N to 31.6°N) compared to V4km.smooth corresponds well with its higher terrain nearby, while the increase occurs where the elevation is higher in the V4km (e.g., 30.7°N to 31.2°N).

Furthermore, precipitation changes are generally located south of the terrain difference between the two experiments. Over the central Himalayas, the relationship between the differences in precipitation and terrain from the two experiments is similar. The impacts of topographical complexity on precipitation over these two regions are mainly due to the narrower and sharper slopes (in the direction perpendicular to the Himalayas) resolved in V4km, which have the effect of shifting the lifted airflow, and hence precipitation, northward compared to V4km.smooth. Rahimi et al. (2019)

also found this northward precipitation shift upon comparing two experiments at different horizontal resolutions. However, over the eastern Himalayas, the abovementioned mechanism seems less evident compared to the other cent-

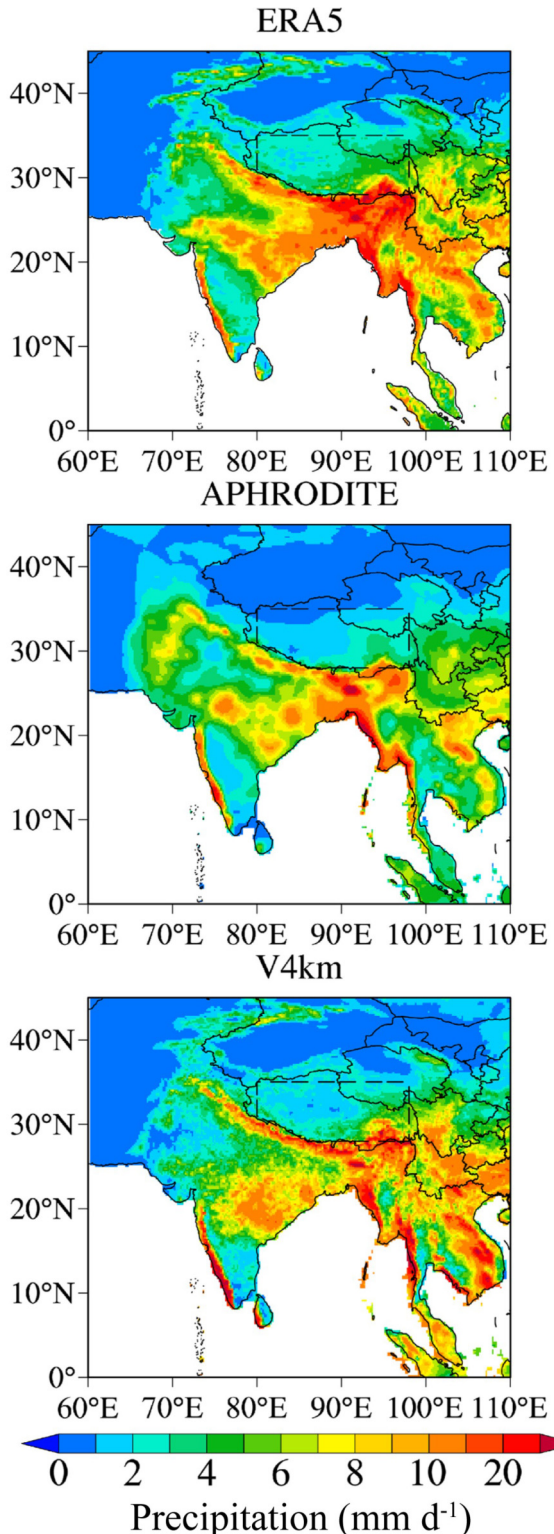


Fig. 9. Spatial distributions of precipitation from the ERA5 reanalysis, APHRODITE observation, and the simulation with the complex topography averaged from 1 June to 31 August 2015.

ral and western regions. This is mainly due to the flow through the Yarlung Tsangpo Grand Canyon exerting a significant impact on moisture transport and precipitation over this region, noting that the canyon is better resolved in V4km than in V4km.smooth. Therefore, the precipitation differences between the two experiments, i.e., higher precipitation in V4km, are mainly attributed to this resolved canyon.

Aside from the precipitation along the direction perpendicular to the Himalayas, the difference in precipitation along the Himalayas over the three regions (denoted by three red dashed lines in Fig. 12) between the two experiments is also analyzed (Fig. 13). Over the western Himalayas, there is a strong correlation between precipitation and terrain height in V4km. The peak precipitation corresponds with mountains and less precipitation occurs in the small-scale valleys (e.g., ~79.8°E, ~81.7°E, and ~82.5°E). However, in V4km.smooth, precipitation is generally higher than in V4km because its terrain is smoothed, and thus the small-scale valleys are not resolved well. Precipitation in V4km.smooth is also higher without fully resolving the valleys over the central (e.g., 92.5°E to 93.2°E) and the eastern (e.g., 95.9°E to 97.1°E, and 97.3°E to 98°E) Himalayas. Therefore, it is evident that the greater number of valleys parallel to the moisture transport across the Himalayas, better resolved by V4km, serve as channels for moisture transport and favor the northward shift of precipitation compared to V4km.smooth.

5. Conclusion and discussion

In this study, a non-hydrostatic global variable-resolution atmospheric model (MPAS-Atmosphere) is used to simulate the characteristics of summer rainfall over the TP at convective-permitting scales. The simulations of key meteorological fields around the TP are evaluated with the reanalysis and observation data. Afterward, the impacts of topographical complexity on the moisture transport and precipitation over the TP are investigated by comparing the two experiments with different topography datasets.

Compared with the observations and reanalysis datasets, the simulation at the convective-permitting scale can well capture the spatial pattern of large-scale circulation in the lower and middle troposphere. Geopotential height is overestimated throughout the region due to simulated warmer temperatures from the lower to middle troposphere. The wind flow into the southern TP in the middle troposphere is somewhat underestimated due to the southward shift of modeled cyclone near the Bay of Bengal. Near-surface temperature, precipitable water, cloud amount, and precipitation around the TP are generally reproduced in the simulation.

In summer, the moisture is mainly transported into the TP through the western and southern boundaries, with the latter contributing the most. The moisture is transported away from the TP mainly through its eastern boundary. The topographical complexity significantly weakens both the moisture inflow and outflow of the TP due to the weakening of

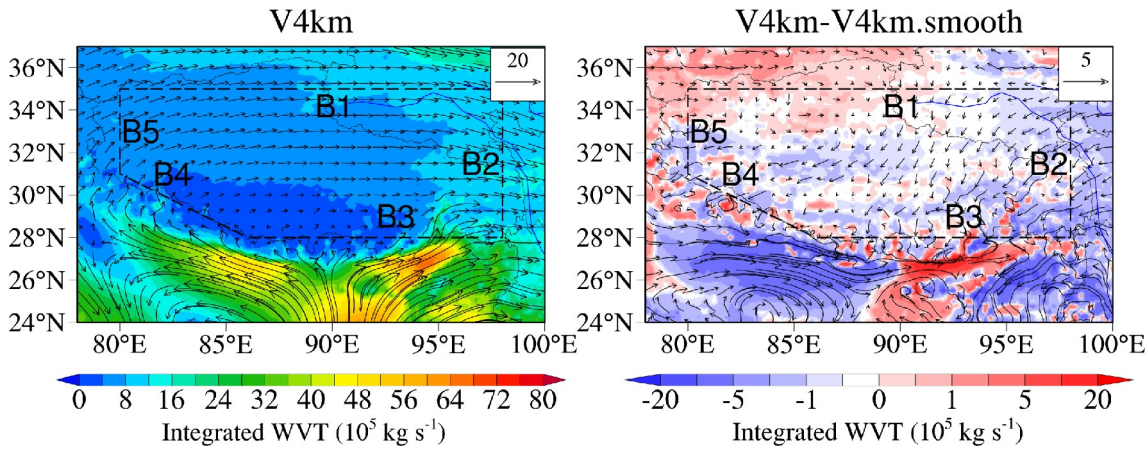


Fig. 10. Spatial distributions of integrated water vapor transport for the simulation with the complex topography averaged from 1 June to 31 August 2015, and the difference between the simulations with the complex and smooth topography.

Table 1. Integrated moisture transport through the five boundaries (denoted in Fig. 2) into the TP. $1 \text{ Tg} = 10^{12} \text{ g}$.

	Moisture transport (Tg h^{-1})	
	V4km	V4km.smooth
B1	-0.2	-10.9
B2	-103.3	-124.6
B3	98.9	117.9
B4	38.0	44.2
B5	26.1	27.4
Sum	59.5	54.0

Table 2. Moisture budget over the TP. $1 \text{ Tg} = 10^{12} \text{ g}$.

	Moisture budget (Tg h^{-1})	
	V4km	V4km.smooth
WVT	59.5	54.0
Evaporation	105.8	103.6
Precipitation	192.2	186.2

the winds below the middle troposphere. Due to topographical complexity, these patterns result in an overall net increase of moisture transport by 11% into the TP. One recent study, conducted in a regional convection-permitting simulation over the TP, found a reduction of net moisture flux in a convection-permitting simulation compared to a simulation using a convective parameterization (Zhao et al., 2021), which was mainly attributed to the up-scale effects of resolved moist convection rather than topographical complexity. Furthermore, the impacts of complex topography on the moisture budget terms over the entire TP are primarily reflected by the moisture transport term, while the impacts on other terms are relatively small.

The primary impacts of topographical complexity on precipitation concentrate on the Himalayas region and are negligible over the TP. Although the changes of precipitation averaged over the entire western or eastern Himalayas by topographical complexity are insignificant, the spatial distributions of precipitation are significantly modulated. On the

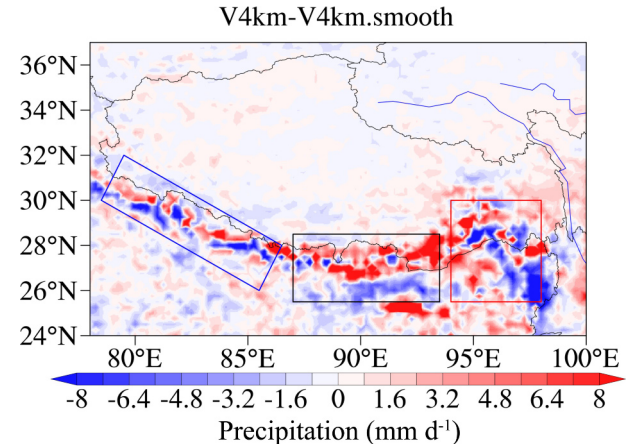


Fig. 11. Spatial distributions of the difference in precipitation between the simulations with the complex and smooth topography averaged from 1 June to 31 August 2015, with the blue rectangular region being the western Himalayas, the black rectangular region being the central Himalayas and the red rectangular region being the eastern Himalayas. Table 3 shows the average precipitation in these areas.

Table 3. The average precipitation over the three Himalayan sub-regions: western, central, and eastern (denoted by blue, black, and red boxes, respectively, in Fig. 11). $1 \text{ Tg} = 10^{12} \text{ g}$.

	Average precipitation (mm d^{-1})	
	V4km	V4km.smooth
Western	9.56	9.78
Central	11.82	10.56
Eastern	14.67	14.69

one hand, the southern slopes of the Himalayas are generally sharper with the complex topography so that they shift the lifted airflow, and hence precipitation, northward compared to the smooth topography. On the other hand, more small-scale valleys are resolved in the experiment with complex topography, which serve as the channels for moisture transport across the Himalayas, also favoring a northward

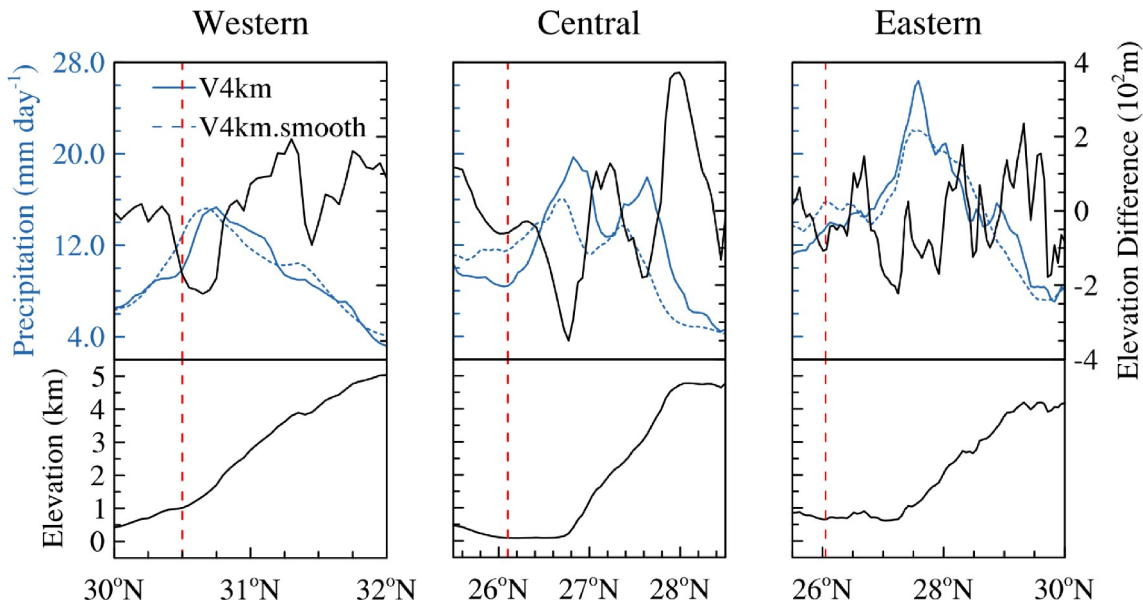


Fig. 12. The precipitation amounts and elevation along the direction perpendicular to the Himalayas for two simulations with complex and smooth topography averaged over the three subregions (denoted by blue, black, and red boxes, respectively, in Fig. 11), from 1 June to 31 August 2015. The X-axis of “western” is the latitude along the northwestern boundary of the blue box in Fig. 11. Blue solid (dashed) lines denote precipitation in V4km (V4km.smooth). Black denotes the elevation difference between two simulations in top plots and denotes elevation from V4km in bottom plots. Red dashed lines in three subregions denote the location of transects analyzed in Fig. 13.

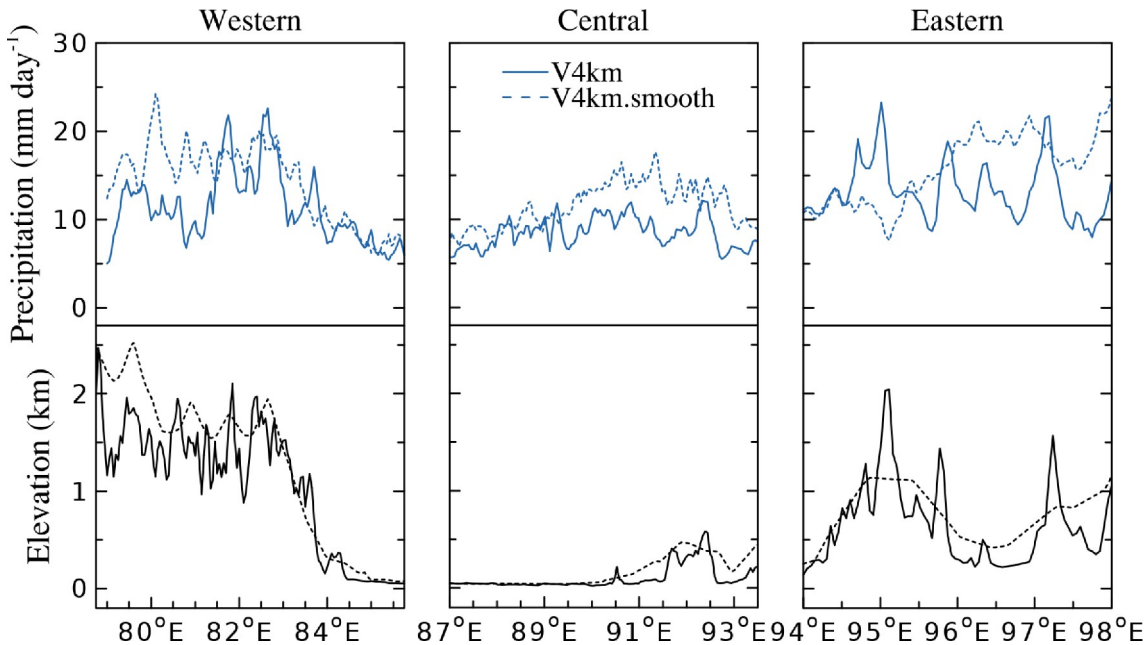


Fig. 13. The precipitation amounts and elevation along the Himalayas (denoted by three red dashed lines in Fig. 12) of two simulations with complex and smooth topography averaged from 1 June to 31 August 2015. Blue solid (dashed) lines denote precipitation in V4km (V4km.smooth), and the black lines denote elevation.

shift of precipitation. Some previous studies with regional modeling at convection-permitting scales found that using high horizontal resolution or including sub-grid turbulent orographic form drag (TOFD) effect could reduce the precipitation over the higher central Himalayas and increase the precipitation over the lower central Himalayas due to its complex topography (e.g., Wang et al., 2020). They focused more on

the TOFD effect of complex topography. In contrast, this study attributed the differences in precipitation between the complex and smooth topography to the different degrees of Himalayan slopes and the extent to which valleys are resolved, partly pointed out by Rahimi et al. (2019).

MPAS-Atmosphere is characterized by a global variable-resolution model which avoids the lateral boundary con-

straint in limited-area simulations. This provides an advantage in researching the influence of complex topography on the large-scale circulation. However, this study conducts the experiments with re-initialization every five days, representing the “instant” impacts of topographical complexity. As a result, the regional feedback from topography may be limited to, at most, a five-day timescale. The abovementioned limitations could possibly be clarified with carefully designed future research plan. For example, a continuous convection-permitting simulation of the whole summer will be conducted in the future to ascertain the climatic effects of the complex topography over the TP region.

Acknowledgements. This research was supported by the National Natural Science Foundation of China NSFC (Grant Nos. 91837310, 42061134009, 41775146), the USTC Research Funds of the Double First-Class Initiative (YD2080002007), and the Strategic Priority Research Program of the Chinese Academy of Sciences (XDB41000000). The study used the computing resources from the High-Performance Computing Center of the University of Science and Technology of China (USTC) and the TH-2 of the National Supercomputer Center in Guangzhou (NSCC-GZ).

Data statement. The release version of MPAS-Atmosphere can be downloaded from <https://doi.org/10.5281/zenodo.4892293>. The meshes used in this study can be downloaded from <http://aemol.ustc.edu.cn/product/list/> or by contacting chunzhao@ustc.edu.cn.

Author contributions. Gudongze LI, Haoming CHEN, Mingyue XU, and Chun ZHAO designed the experiments and conducted and analyzed the simulations. All authors contributed to the discussion and final version of the paper.

Open Access This article is licensed under a Creative Commons Attribution 4.0 International License, which permits use, sharing, adaptation, distribution and reproduction in any medium or format, as long as you give appropriate credit to the original author(s) and the source, provide a link to the Creative Commons licence, and indicate if changes were made. The images or other third party material in this article are included in the article’s Creative Commons licence, unless indicated otherwise in a credit line to the material. If material is not included in the article’s Creative Commons licence and your intended use is not permitted by statutory regulation or exceeds the permitted use, you will need to obtain permission directly from the copyright holder. To view a copy of this licence, visit <http://creativecommons.org/licenses/by/4.0/>.

Electronic supplementary material: Supplementary material is available in the online version of this article at <https://doi.org/10.1007/s00376-022-1409-7>.

REFERENCES

- Barnett, T. P., J. C. Adam, and D. P. Lettenmaier, 2005: Potential impacts of a warming climate on water availability in snow-dominated regions. *Nature*, **438**, 303–309, <https://doi.org/10.1038/nature04141>.
- Boos, W. R., and Z. M. Kuang, 2010: Dominant control of the South Asian monsoon by orographic insulation versus plateau heating. *Nature*, **463**, 218–222, <https://doi.org/10.1038/nature08707>.
- Boos, W. R., and Z. M. Kuang, 2013: Sensitivity of the South Asian monsoon to elevated and non-elevated heating. *Scientific Reports*, **3**, 1192, <https://doi.org/10.1038/srep01192>.
- Burbank, D. W., B. Bookhagen, E. J. Gabet, and J. Putkonen, 2012: Modern climate and erosion in the Himalaya. *Comptes Rendus Geoscience*, **344**, 610–626, <https://doi.org/10.1016/j.crte.2012.10.010>.
- Chen, F., and J. Dudhia, 2001: Coupling an advanced land surface-hydrology model with the Penn state-NCAR MM5 modeling system. *Part I: Model implementation and sensitivity*. *Mon. Wea. Rev.*, **129**, 569–585, [https://doi.org/10.1175/1520-0493\(2001\)129<0569:CAALSH>2.0.CO;2](https://doi.org/10.1175/1520-0493(2001)129<0569:CAALSH>2.0.CO;2).
- Duan, A. M., and G. X. Wu, 2005: Role of the Tibetan Plateau thermal forcing in the summer climate patterns over subtropical Asia. *Climate Dyn.*, **24**, 793–807, <https://doi.org/10.1007/s00382-004-0488-8>.
- Feng, L., and T. J. Zhou, 2012: Water vapor transport for summer precipitation over the Tibetan Plateau: Multidata set analysis. *J. Geophys. Res.*, **117**, D20114, <https://doi.org/10.1029/2011JD017012>.
- Gao, Y. H., L. Cuo, and Y. X. Zhang, 2014: Changes in moisture flux over the Tibetan Plateau during 1979–2011 and possible mechanisms. *J. Climate*, **27**, 1876–1893, <https://doi.org/10.1175/JCLI-D-13-00321.1>.
- Gao, Y. H., J. W. Xu, and D. L. Chen, 2015: Evaluation of WRF mesoscale climate simulations over the Tibetan Plateau during 1979–2011. *J. Climate*, **28**, 2823–2841, <https://doi.org/10.1175/JCLI-D-14-00300.1>.
- Gu, H. H., Z. B. Yu, W. R. Peltier, and X. Y. Wang, 2020: Sensitivity studies and comprehensive evaluation of RegCM4.6.1 high-resolution climate simulations over the Tibetan Plateau. *Climate Dyn.*, **54**, 3781–3801, <https://doi.org/10.1007/s00382-020-05205-6>.
- Hagos, S., L. R. Leung, Q. Yang, C. Zhao, and J. Lu, 2015: Resolution and dynamical core dependence of atmospheric river frequency in global model simulations. *J. Climate*, **28**, 2764–2776, <https://doi.org/10.1175/JCLI-D-14-00567.1>.
- Hersbach, H., and Coauthors, 2020: The ERA5 global reanalysis. *Quart. J. Roy. Meteor. Soc.*, **146**, 1999–2049, <https://doi.org/10.1002/qj.3803>.
- Hong, S. Y., 2010: A new stable boundary-layer mixing scheme and its impact on the simulated East Asian summer monsoon. *Quart. J. Roy. Meteor. Soc.*, **136**, 1481–1496, <https://doi.org/10.1002/qj.665>.
- Hong, S.-Y., and J.-O. J. Lim, 2006: The WRF single-moment 6-class microphysics scheme (WSM6). *Journal of the Korean Meteorological Society*, **42**, 129–151.
- Iacono, M. J., E. J. Mlawer, S. A. Clough, and J.-J. Morcrette, 2000: Impact of an improved longwave radiation model, RRTM, on the energy budget and thermodynamic properties of the NCAR community climate model, CCM3. *J. Geophys. Res.*, **105**, 1 4873–1 4890, <https://doi.org/10.1029/2000JD900091>.
- Immerzeel, W. W., L. P. H. Van Beek, and M. F. P. Bierkens, 2010: Climate change will affect the Asian water towers. *Science*, **328**, 1382–1385, <https://doi.org/10.1126/science.1183188>.
- Judit, F., 2018: Insights into atmospheric predictability through

- global convection-permitting model simulations. *J. Atmos. Sci.*, **75**, 1477–1497, <https://doi.org/10.1175/JAS-D-17-0343.1>.
- Karki, R., S. ul Hasson, L. Gerlitz, U. Schickhoff, T. Scholten, and J. Böhner, 2017: Quantifying the added value of convection-permitting climate simulations in complex terrain: A systematic evaluation of WRF over the Himalayas. *Earth System Dynamics*, **8**, 507–528, <https://doi.org/10.5194/esd-8-507-2017>.
- Klemp, J. B., 2011: A terrain-following coordinate with smoothed coordinate surfaces. *Mon. Wea. Rev.*, **139**, 2163–2169, <https://doi.org/10.1175/MWR-D-10-05046.1>.
- Klemp, J. B., W. C. Skamarock, and J. Dudhia, 2007: Conservative split-explicit time integration methods for the compressible nonhydrostatic equations. *Mon. Wea. Rev.*, **135**, 2897–2913, <https://doi.org/10.1175/MWR3440.1>.
- Kobayashi, S., and Coauthors, 2015: The JRA-55 reanalysis: General specifications and basic characteristics. *J. Meteor. Soc. Japan*, **93**, 5–48, <https://doi.org/10.2151/jmsj.2015-001>.
- Landu, K., L. R. Leung, S. Hagos, V. Vinoj, S. A. Rauscher, T. Ringler, and M. Taylor, 2014: The dependence of ITCZ structure on model resolution and dynamical core in aquaplanet simulations. *J. Climate*, **27**, 2375–2385, <https://doi.org/10.1175/JCLI-D-13-00269.1>.
- Li, P. X., K. Furtado, T. J. Zhou, H. M. Chen, and J. Li, 2021: Convection-permitting modelling improves simulated precipitation over the central and eastern Tibetan Plateau. *Quart. J. Roy. Meteor. Soc.*, **147**, 341–362, <https://doi.org/10.1002/qj.3921>.
- Lin, C. G., D. L. Chen, K. Yang, and T. H. Ou, 2018: Impact of model resolution on simulating the water vapor transport through the central Himalayas: Implication for models' wet bias over the Tibetan Plateau. *Climate Dyn.*, **51**, 3195–3207, <https://doi.org/10.1007/s00382-018-4074-x>.
- Lutz, A. F., W. W. Immerzeel, A. B. Shrestha, and M. F. P. Bierkens, 2014: Consistent increase in High Asia's runoff due to increasing glacier melt and precipitation. *Nature Climate Change*, **4**, 587–592, <https://doi.org/10.1038/nclimate2237>.
- Ma, J. H., H. J. Wang, and K. Fan, 2015: Dynamic downscaling of summer precipitation prediction over China in 1998 using WRF and CCSM4. *Adv. Atmos. Sci.*, **32**, 577–584, <https://doi.org/10.1007/s00376-014-4143-y>.
- Mlawer, E. J., S. J. Taubman, P. D. Brown, M. J. Iacono, and S. A. Clough, 1997: Radiative transfer for inhomogeneous atmospheres: RRTM, a validated correlated-k model for the long-wave. *J. Geophys. Res.*, **102**, 16 663–1 6682, <https://doi.org/10.1029/97JD00237>.
- O'Brien, T. A., F. Y. Li, W. D. Collins, S. A. Rauscher, T. D. Ringler, M. Taylor, S. M. Hagos, and L. R. Leung, 2013: Observed scaling in clouds and precipitation and scale incognizance in regional to global atmospheric models. *J. Climate*, **26**, 9313–9333, <https://doi.org/10.1175/JCLI-D-13-0005.1>.
- O'Brien, T. A., W. D. Collins, K. Kashinath, O. Rübel, S. Byna, J. M. Gu, H. Krishnan, and P. A. Ullrich, 2016: Resolution dependence of precipitation statistical fidelity in hindcast simulations. *Journal of Advances in Modeling Earth Systems*, **8**, 976–990, <https://doi.org/10.1002/2016MS000671>.
- Qiu, J., 2008: China: The third pole. *Nature*, **454**, 393–396, <https://doi.org/10.1038/454393a>.
- Rahimi, S. R., C. L. Wu, X. H. Liu, and H. Brown, 2019: Exploring a variable-resolution approach for simulating regional climate over the Tibetan Plateau using VR-CESM. *J. Geophys. Res.*, **124**, 4490–4513, <https://doi.org/10.1029/2018JD028925>.
- Ringler, T. D., D. Jacobsen, M. Gunzburger, L. L. Ju, M. Duda, and W. Skamarock, 2011: Exploring a multiresolution modeling approach within the shallow-water equations. *Mon. Wea. Rev.*, **139**, 3348–3368, <https://doi.org/10.1175/MWR-D-10-05049.1>.
- Ringler, T. D., L. Ju, and M. Gunzburger, 2008: A multiresolution method for climate system modeling: application of spherical centroidal Voronoi tessellations. *Ocean Dynamics*, **58**, 475–498, <https://doi.org/10.1007/s10236-008-0157-2>.
- Sakaguchi, K., and Coauthors, 2015: Exploring a multiresolution approach using AMIP simulations. *J. Climate*, **28**, 5549–5574, <https://doi.org/10.1175/JCLI-D-14-00729.1>.
- Sakaguchi, K., J. Lu, L. R. Leung, C. Zhao, Y. J. Li, and S. Hagos, 2016: Sources and pathways of the upscale effects on the Southern Hemisphere jet in MPAS-CAM4 variable-resolution simulations. *Journal of Advances in Modeling Earth Systems*, **8**, 1786–1805, <https://doi.org/10.1002/2016MS000743>.
- Sandu, I., P. Bechtold, A. Beljaars, A. Bozzo, F. Pithan, T. G. Shepherd, and A. Zadra, 2016: Impacts of parameterized orographic drag on the Northern Hemisphere winter circulation. *Journal of Advances in Modeling Earth Systems*, **8**, 196–211, <https://doi.org/10.1002/2015MS000564>.
- Shen, C., J. L. Zha, J. Wu, D. M. Zhao, C. Azorin-Molina, W. X. Fan, and Y. Yu, 2022: Does CRA-40 outperform other reanalysis products in evaluating near-surface wind speed changes over China. *Atmospheric Research*, **266**, 105948, <https://doi.org/10.1016/j.atmosres.2021.105948>.
- Shen, M. G., S. L. Piao, N. Cong, G. X. Zhang, and I. A. Jassens, 2015: Precipitation impacts on vegetation spring phenology on the Tibetan Plateau. *Global Change Biology*, **21**, 3647–3656, <https://doi.org/10.1111/gcb.12961>.
- Singh, P., and L. Bengtsson, 2004: Hydrological sensitivity of a large Himalayan basin to climate change. *Hydrological Processes*, **18**, 2363–2385, <https://doi.org/10.1002/hyp.1468>.
- Skamarock, W. C., and J. B. Klemp, 2008: A time-split nonhydrostatic atmospheric model for weather research and forecasting applications. *J. Comput. Phys.*, **227**, 3465–3485, <https://doi.org/10.1016/j.jcp.2007.01.037>.
- Skamarock, W. C., J. B. Klemp, M. G. Duda, L. D. Fowler, S.-H. Park, and T. D. Ringler, 2012: A multiscale nonhydrostatic atmospheric model using centroidal voronoi tesselations and c-grid staggering. *Mon. Wea. Rev.*, **140**, 3090–3105, <https://doi.org/10.1175/MWR-D-11-00215.1>.
- Su, F. G., X. L. Duan, D. L. Chen, Z. C. Hao, and L. Cuo, 2013: Evaluation of the global climate models in the CMIP5 over the Tibetan Plateau. *J. Climate*, **26**, 3187–3208, <https://doi.org/10.1175/JCLI-D-12-00321.1>.
- Sun, R. C., H. L. Yuan, X. L. Liu, and X. M. Jiang, 2016: Evaluation of the latest satellite–gauge precipitation products and their hydrologic applications over the Huaihe River basin. *J. Hydrol.*, **536**, 302–319, <https://doi.org/10.1016/j.jhydrol.2016.02.054>.
- Thompson, G., P. R. Field, R. M. Rasmussen, and W. D. Hall, 2008: Explicit forecasts of winter precipitation using an improved bulk microphysics scheme. Part II: Implementation of a new snow parameterization. *Mon. Wea. Rev.*, **136**, 5095–5115, <https://doi.org/10.1175/2008MWR2387.1>.
- Tian, L. D., T. D. Yao, K. MacClune, J. W. C. White, A. Schilla, B. Vaughn, R. Vachon, and K. Ichiyangagi, 2007: Stable isotopic variations in west China: A consideration of moisture sources. *J. Geophys. Res.*, **112**, D10112, <https://doi.org/10.1029/2006JD007718>.

- Wang, Y., and Coauthors, 2020: Synergy of orographic drag parameterization and high resolution greatly reduces biases of WRF-simulated precipitation in central Himalaya. *Climate Dyn.*, **54**, 1729–1740, <https://doi.org/10.1007/s00382-019-05080-w>.
- Wu, G. X. and Coauthors, 2007: The influence of mechanical and thermal forcing by the Tibetan Plateau on Asian climate. *Journal of Hydrometeorology*, **8**, 770–789, <https://doi.org/10.1175/JHM609.1>.
- Wu, G. X., Y. M. Liu, B. W. Dong, X. Y. Liang, A. M. Duan, Q. Bao, and J. J. Yu, 2012: Revisiting Asian monsoon formation and change associated with Tibetan Plateau forcing: I. Formation. *Climate Dyn.*, **39**, 1169–1181, <https://doi.org/10.1007/s00382-012-1334-z>.
- Wu, G. X., and Coauthors, 2015: Tibetan Plateau climate dynamics: Recent research progress and outlook. *National Science Review*, **2**, 100–116, <https://doi.org/10.1093/nsr/nwu045>.
- Xu, J. W., and Coauthors, 2018: On the role of horizontal resolution over the Tibetan Plateau in the REMO regional climate model. *Climate Dyn.*, **51**, 4525–4542, <https://doi.org/10.1007/s00382-018-4085-7>.
- Xu, M. Y., and Coauthors, 2021: Convection-permitting hindcasting of diurnal variation of Mei-yu rainfall over East China with a global variable-resolution model. *J. Geophys. Res.*, **126**, e2021JD034823, <https://doi.org/10.1029/2021JD034823>.
- Xu, X. D., C. G. Lu, X. H. Shi, and S. T. Gao, 2008: World water tower: An atmospheric perspective. *Geophys. Res. Lett.*, **35**, L20815, <https://doi.org/10.1029/2008GL035867>.
- Xu, Y., X. J. Gao, and F. Giorgi, 2010: Upgrades to the reliability ensemble averaging method for producing probabilistic climate-change projections. *Climate Research*, **41**, 61–81, <https://doi.org/10.3354/cr00835>.
- Xue, H. L., X. S. Shen, and Y. Su, 2011: Parameterization of turbulent orographic form drag and implementation in GRAPES. *Journal of Applied Meteorological Science*, **22**, 169–181, <https://doi.org/10.3969/j.issn.1001-7313.2011.02.006>.
- Yanai, M., and G.-X. Wu, 2006: Effects of the Tibetan Plateau. *The Asian Monsoon*, B. Wang, Ed., Springer, 513–549, https://doi.org/10.1007/3-540-37722-0_13.
- Yang, K., B. S. Ye, D. G. Zhou, B. Y. Wu, T. Foken, J. Qin, and Z. Y. Zhou, 2011: Response of hydrological cycle to recent climate changes in the Tibetan Plateau. *Climatic Change*, **109**, 517–534, <https://doi.org/10.1007/s10584-011-0099-4>.
- Yang, Q., L. R. Leung, S. A. Rauscher, T. D. Ringler, and M. A. Taylor, 2014: Atmospheric moisture budget and spatial resolution dependence of precipitation extremes in aquaplanet simulations. *J. Climate*, **27**, 3565–3581, <https://doi.org/10.1175/JCLI-D-13-00468.1>.
- Yao, B., C. Liu, Y. Yin, Z. Q. Liu, C. X. Shi, H. Iwabuchi, and F. Z. Weng, 2020: Evaluation of cloud properties from reanalyses over East Asia with a radiance-based approach. *Atmospheric Measurement Techniques*, **13**, 1033–1049, <https://doi.org/10.5194/amt-13-1033-2020>.
- Yao, T. D., and Coauthors, 2012: Different glacier status with atmospheric circulations in Tibetan Plateau and surroundings. *Nature Climate Change*, **2**, 663–667, <https://doi.org/10.1038/nclimate1580>.
- Yatagai, A., P. Xie, and P. Alpert, 2008: Development of a daily gridded precipitation data set for the Middle East. *Advances in Geosciences*, **12**, 165–170, <https://doi.org/10.5194/adgeo-12-165-2008>.
- Yatagai, A., K. Kamiguchi, O. Arakawa, A. Hamada, N. Yasutomi, and A. Kitoh, 2012: APHRODITE: Constructing a long-term daily gridded precipitation dataset for Asia based on a dense network of rain gauges. *Bull. Amer. Meteor. Soc.*, **93**, 1401–1415, <https://doi.org/10.1175/BAMS-D-11-00122.1>.
- Ye, D.-Z., and G. X. Wu, 1998: The role of the heat source of the Tibetan Plateau in the general circulation. *Meteorol. Atmos. Phys.*, **67**, 181–198, <https://doi.org/10.1007/BF01277509>.
- Yu, X. J., L. X. Zhang, T. J. Zhou, and J. W. Liu, 2021: The Asian subtropical westerly jet stream in CRA-40, ERA5, and CFSR reanalysis data: Comparative assessment. *J. Meteor. Res.*, **35**, 46–63, <https://doi.org/10.1007/s13351-021-0107-1>.
- Zhang, C., Q. H. Tang, and D. L. Chen, 2017: Recent changes in the moisture source of precipitation over the Tibetan Plateau. *J. Climate*, **30**, 1807–1819, <https://doi.org/10.1175/JCLI-D-15-0842.1>.
- Zhang, M. X., and Coauthors, 2020: Impact of topography on black carbon transport to the southern Tibetan Plateau during the pre-monsoon season and its climatic implication. *Atmospheric Chemistry and Physics*, **20**, 5923–5943, <https://doi.org/10.5194/acp-20-5923-2020>.
- Zhang, R. H., T. Koike, X. D. Xu, Y. M. Ma, and K. Yang, 2012: A China-Japan cooperative JICA atmospheric observing network over the Tibetan Plateau (JICA/Tibet Project): An overview. *J. Meteor. Soc. Japan*, **90**, 1–16, <https://doi.org/10.2151/jmsj.2012-C01>.
- Zhao, B., B. Zhang, C. X., Shi, and J. W. Liu, 2019a: Comparison of the global energy cycle between Chinese reanalysis interim and ECMWF reanalysis. *Journal of Meteorological Research*, **33**, 563–575, <https://doi.org/10.1007/s13351-019-8129-7>.
- Zhao, C., and Coauthors, 2016: Exploring the impacts of physics and resolution on aqua-planet simulations from a nonhydrostatic global variable-resolution modeling framework. *Journal of Advances in Modeling Earth Systems*, **8**, 1751–1768, <https://doi.org/10.1002/2016MS000727>.
- Zhao, C., and Coauthors, 2019b: Modeling extreme precipitation over East China with a global variable-resolution modeling framework (MPASv5.2): Impacts of resolution and physics. *Geoscientific Model Development*, **12**, 2707–2726, <https://doi.org/10.5194/gmd-12-2707-2019>.
- Zhao, P., X. J. Zhou, J. M. Chen, G. Liu, and S. L. Nan, 2019c: Global climate effects of summer Tibetan Plateau. *Science Bulletin*, **64**, 1–3, <https://doi.org/10.1016/j.scib.2018.11.019>.
- Zhao, Y., and T. J. Zhou, 2020: Asian water tower evinced in total column water vapor: A comparison among multiple satellite and reanalysis data sets. *Climate Dyn.*, **54**, 231–245, <https://doi.org/10.1007/s00382-019-04999-4>.
- Zhao, Y., T. J. Zhou, P. X. Li, K. Furtado, and L. W. Zou, 2021: Added value of a convection permitting model in simulating atmospheric water cycle over the Asian Water Tower. *J. Geophys. Res.*, **126**, e2021JD034788, <https://doi.org/10.1029/2021JD034788>.
- Zhou, X., A. Beljaars, Y. Wang, B. Huang, C. Lin, Y. Chen, and H. Wu, 2017: Evaluation of WRF simulations with different selections of subgrid orographic drag over the Tibetan Plateau. *J. Geophys. Res.*, **122**, 9759–9772, <https://doi.org/10.1002/2017JD027212>.
- Zhu, Y.-Y., and S. N. Yang, 2020: Evaluation of CMIP6 for historical temperature and precipitation over the Tibetan Plateau and its comparison with CMIP5. *Advances in Climate Change Research*, **11**, 239–251, <https://doi.org/10.1016/j.accre.2020.08.001>.